Analysis of Proximitized Molybdenum-Copper Superconducting Bilayers

by

Cameron Kopas

A Thesis Presented in Partial Fulfillment
of the Requirements for the Degree
Master of Science

Approved July 2014 by the
Graduate Supervisory Committee:

Nathan Newman, Chair
Rakesh Singh
Ralph Chamberlin

ARIZONA STATE UNIVERSITY

August 2014

ABSTRACT

A series of Molybdenum-Copper bilayers were studied for use in 120mK superconducting transition edge sensors for spectrometer applications. The Transition temperature (T_C) was tuned to the desired temperature using the proximity effect, by adjusting the thickness of a normal copper layer in direct contact with the superconducting molybdenum layer in a proximitized bilayer structure. The bilayers have a fixed normal metal thickness $d_{Cu} \approx 1250$Å, on top of a variable superconductor thickness 650Å $\leq d_{Mo} \leq$ 1000Å. Material characterization techniques including X-ray Diffraction (XRD), Rutherford Backscattering Spectroscopy (RBS), Atomic Force Microscopy (AFM), and 4-point electrical characterization are used to characterize the films. Film T_C are compared with the results of the Usadel proximity theory. The results of RBS analysis demonstrated that some Argon-contamination is observed at the Mo film-substrate interface, which correlates with bilayer surface roughness (as observed with AFM), reduced crystalline quality (via XRD Rocking Curve), and a deviation from the theoretical expected T_C for a bilayer. The Argon contamination is presumably the cause of interface roughness, reducing the interface transmission coefficient in the Usadel model, and producing the discrepancy from the expected T_C.

ACKNOWLEDGEMENT

Thank you to Dr. Nathan Newman, for guidance along the entire investigation, and support in revising this document; Dr. Rakesh Singh for assistance in initial characterization; Dr. Mengchu Huang for AFM measurements; Dr. Robin Cantor and Dr. Ad Hall of Star CryoElectronics in Santa Fe, New Mexico, for the inspiration, support, and sample production for this investigation.

TABLE OF CONTENTS

Page

LIST OF TABLES v

LIST OF FIGURES vi

CHAPTER

1. INTRODUCTION 1

Background 1

The Transition Edge Sensor 1

The Superconducting Proximity Effect 2

Objectives 2

Research Outline 3

2. METHODS 4

Materials Selection 4

Film Preperation 4

Electrical Characterization 6

RBS Characterization 8

XRD Characterization 12

Atomic Force Microscopy 14

Theoretical T_C Modeling 15

CHAPTER Page

3. RESULTS & DISCUSSION....17

Electrical Characterization.... 17

Rutherford Backscattering Spectroscopy (RBS) 19

X-ray Diffraction 22

Atomic Force Microscopy (AFM).... 24

T_C Simulation.... 26

4. CONCLUSIONS....28

REFERENCES 30

LIST OF TABLES

Table Page

1: Mo Thickness and Resistivity Ratio (RRR) 17

2: Measured Superconducting Transition Remperatures (T_C) 18

3: Thickness and Ar Content for Each Film Bilayer via RBS.. 19

4: RMS Surface Roughness for Each Film Bilayer, via AFM... 24

LIST OF FIGURES

Figure Page

1: Schematic Diagram of a Sputter Vacuum System. 5

2: Cartoon of an Idealized ρ –T Curve for a Superconducting Metal 6

3: Schematic Diagram of the RBS Experimental Chamber 8

4: Diagrams of the X-ray Diffraction Scan Configuration 13

5: Simulated RBS Data for Mo 900, Showing Argon 19

6: Plot of Bilayer T_C and Argon Content from RBS 20

7: Plot of Rocking Curve FWHM for Cu (111) and Argon Content 22

8: XRD Rocking Curve Data for the Cu (111) Peaks. 22

9: The θ-2θ Powder X-ray Diffraction Plots for Each Film Bilayer 23

10: 3-D AFM Images for Unifilm Mo 680 and 900 25

11: Plot of RMS Surface Roughness and Measured Argon Content 25

13: Plot of t Against Ar, RMS Roughness, and Rocking Curve FWHM 27

12:Usadel Simulations for Each Bilayer. 26

CHAPTER 1

INTRODUCTION

BACKGROUND

THE TRANSITION EDGE SENSOR

The development of more and more sensitive detectors is paramount to the advancement of characterization techniques used in modern research. Among these, one of the most sensitive detector schemes is the Transition Edge Sensor (TES). This sensor takes advantage of the strong temperature dependence of the Superconducting Transition Temperature (T_C), the narrow transition width, and the large change in resistivity between the superconducting and normal metal states. The device is operated at a temperature within the narrow T_C temperature region (where $\Delta R/\Delta T$ is large). Energy from X-ray photons being absorbed into the device will raise the temperature, then a drastic change in resistance occurs, and is easily measured, allowing for easy detection of individual photons. These detectors are used—for example—in some radio astronomy telescopes, such as the SCUBA-2 Detector in the James Clerk Maxwell Telescope, and in very advanced Energy Dispersive X-ray Spectroscopy (EDX) detectors for material characterization in Scanning Electron Microscopes (SEM).

The Full Width Half Max (FWHM) energy width (lower width refers to improved resolution) is linearly dependent on T_C, with the relation [1]:

$$\Delta \mathrm{E}_{\mathrm{FWHM}} = 2.355\sqrt{\mathrm{k}_{\mathrm{C}} * \mathrm{T}_c^2 \mathrm{C}} \quad (1)$$

Where k_B is Boltzmann's constant, and C is the heat capacity of the material. Improved energy resolution is obtained with lower T_C superconductors, with their smaller Cooper-Pair binding energies. Thus, a low T_C is desirable to make devices that are more sensitive. Unfortunately, many of the lower T_C metals are very reactive and unsuitable for long-term use in stable devices. A clever alternate method is to utilize proximitized bilayers comprised of relatively unreactive components to achieve the desired low temperature superconductor transition [2].

THE SUPERCONDUCTING PROXIMITY EFFECT

The superconducting Proximity effect was described by Werthamer [3] in his 1963 paper. This effect describes how the T_C of superconductor-normal metal bilayers can be changed depending on the ratio of layer thicknesses, the quality of the interface, and the coherence length of the normal metal ξ_N (which is proportional to the mean free path λ_N). Usadel [4] developed a proximity model based on the diffusion of superconducting Cooper Pair electrons from the superconductor into the normal metal (up to the coherence length ξ_N), and diffusion of normal electrons from the normal metal into the superconductor.

OBJECTIVES

This goal of this investigation is to study the chemical, structural, and electrical properties of films produced by our collaborators at Star CryoElectronics to better understand the unexpected T_C deviations from theoretical models. If successful, this will assist in the development of a process for the reliable manufacture of Mo/Cu metallic film bilayers with the desired superconducting transition temperature, T_C, of 120mK.

RESEARCH OUTLINE

At the beginning of this study, Mo/Cu film bilayers were grown by Star CryoElectronics with a process similar to that previously described in the literature [5]. Measurements of these samples' electrical properties yielded an unexplained variation in T_C between with samples grown under similar conditions.

In order to choose appropriate growth parameters, characterize any contaminants, and refine film quality, a systematic set of single-layer Mo and Cu films were grown via DC Sputtering on SiO_2. In order to obtain optimum T_C reduction, Cu layers must have a long coherence length, and the normal metal layer must be at least twice the coherence length, ξ, thick. To ensure that $\xi_{Cu} \geq 1000$Å the samples resistivity ratio, RRR, must be ≥ 10 [6]. Subsequently, Mo/Cu bilayers were grown at different temperatures, and annealed to determine whether layer intermixing will occur. Through these steps a Copper thickness of $d_{Cu} \approx 2100 \pm 50$Å ($\approx 2\xi_{Cu}$), and Molybdenum layers 650Å$\leq d_{Mo} \leq$1000Å were selected for these studies.

Finally, a series of Molybdenum/Copper film bilayers were grown with the selected thicknesses to determine a Mo thickness that will achieve a final device T_C of 120mK.

CHAPTER 2

METHODS

The methods section describes methodologies used for sample preparation, characterization, and analysis. Techniques are discussed in the order that they were performed.

MATERIALS SELECTION

The materials selection, Molybdenum for the superconducting metal and Copper for the normal metal, is based on the need for a $T_C \approx 120mK$, and the stability of the Mo-Cu system. [5] There are some metals with T_C near the desired temperature, for example Hafnium has T_C (Hf) =128mK, and T_C (Ti) ≈400mK, however these materials are more difficult to work with, and are more reactive than Mo with Oxygen and other environmental gases. Any change in composition through reaction with the device would alter the electrical properties of the devices. Therefore, the choice to use a T_C -depressed proximity bilayer scheme is useful for this application. Mo has a bulk T_C of 900mK [7], no allotropes, a similar lattice constant to the SiN substrate (3.14Å), and the Mo/Cu system does not form any metallic alloys under 1000°C [8].

FILM PREPARATION - SPUTTERING

Film and bilayer growth was performed at STAR CryoElectronics in Santa Fe, New Mexico. Films were prepared by DC sputtering.

For this growth technique, the substrates, Silicon (100) wafers cut to 1cm squares, or 4" diameter Si (100) wafers, are affixed to a heater using a heat conductive paste (generally silver paste) and placed in a UHV Chamber. The chamber is evacuated to a pressure typically on the order of 10^{-8} Torr or better. This initial vacuum evacuation removes atmospheric contaminants from the system before the growth. In order to perform sputter deposition, the chamber is then backfilled with ~5-10mT of Argon gas, then the DC sputter source uses a high voltage to generate Argon plasma between the anodic shield, and the cathode target. A permanent magnet behind the sputter target confines the plasma to the target surface, sputtering material from the target out onto the substrate where they are deposited. This technique is useful for depositing materials at deposition rates that can be controlled by the power applied to the gun and the pressure in the chamber.

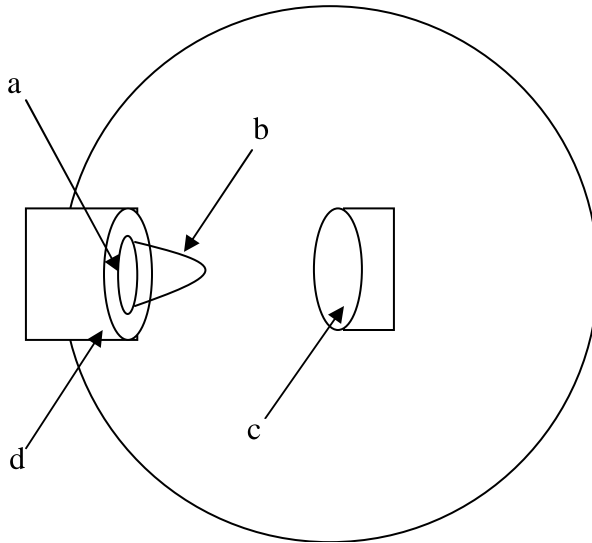

Figure 1: Schematic diagram of a sputter vacuum system. Argon ions impact the target surface and sputter material onto the substrate (a) target material, cathode (b) Argon plasma magnetically confined (c) substrate or wafer heater (d) anode/shield

ELECTRICAL CHARACTERIZATION

SUPERCONDUCTING TRANSITION TEMPERATURE (T_C) MEASUREMENTS

The quickest way to measure T_C of a superconductor using a probe dipped into liquid nitrogen (minimum of 77K for high temperature superconductors), or liquid Helium (lambda point temperature of 2.1K is low enough for most metallic superconductors). However, to reach temperatures below 2.1K for low-T_C materials, a Helium-3 insert, dilution refrigerator or cryostat is necessary. T_C measurements on the film bilayers were performed by NIST in Boulder, Colorado down to 50mK by using a dilution refrigerator.

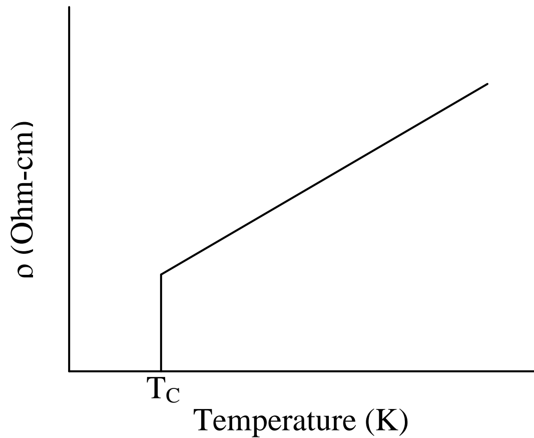

Figure 2: Cartoon of an idealized ρ –T curve for a superconducting metal. The resistivity sharply drops to zero at the transition temperature, T_C

Electrical contacts in the Van der Pauw four-point configuration are used to measure resistivity. In this setup, an Ohmic contact is made at each corner of a 1cmx1cm square sample, and current flows across one edge of the square while voltage is measured across the opposite side. This four-point measurement configuration removes the contributions from resistance in the circuit or at the contacts, so only the properties of the metal layers are measured.

RESIDUAL RESISTIVITY RATIO (RRR) MEASUREMENTS

The Residual resistivity Ratio (RRR) gives a relative metric of film quality, because in the low temperature region impurity and defect scattering dominate the conductivity, while at high temperature phonon scattering dominates. Therefore, a higher RRR suggests that the material has fewer defects and scattering sites, so is of higher quality.

RRR is a measurement which compares the ratio of sample resistivity at room temperature (T≈300 K) and (ideally) T=0 K, where T=4.2 K (the temperature of Liquid Helium at atmospheric pressure) is often used as an approximation for 0K for the sake of practicality. In the case of superconducting materials with T_C above 4.2K, the lower resistivity point is taken from just above the superconducting transition temperature.

Low resistivity at 4.2K and a high resistivity ratio are important properties for device properties of a transition edge sensor. The thermalization temperature limits the frequency at which the device can be read, so a low τ_{therm} is desirable. This thermalization time (minimum time required for the device to reach steady state and allow for a uniform measurement across the device area) is directly proportional to the resistivity of the film by [6]:

$$\tau_{therm} = Ae^2 n(E_f)\rho \quad (2)$$

Where A is the area of the device. The RRR corresponds to the mean free path of a thick film at a low temperature T, via the approximate relation: [9]

$$\lambda_T = RRR_{bulk}\lambda_{300} \quad (3)$$

Then this can be converted to the thin film mean free path, Λ, using [10]

$$\Lambda = \frac{3d}{4}(\ln\left(\frac{\lambda_T}{d}\right) + 0.423) \quad (4)$$

This Λ is related to the coherence length in the clean and dirty limits, respectively [9]:

$$\xi_{clean} = \left(\frac{1}{\xi_0} + \frac{1}{\Lambda}\right)^{-1} \qquad \xi_{dirty} = \sqrt{\frac{\xi_0 \Lambda}{3}} \quad (5\text{ a, b})$$

The material is considered to be in the clean limit if the mean free path is much larger than the coherence length, and in the dirty limit if the mean free path is much lower than coherence length. This coherence length is intuitively the "size" of a cooper pair and in BCS Theory is:

$$\xi = \frac{2\hbar v_f}{\pi \Delta} \quad (6)$$

Where v_f is the Fermi velocity, and Δ is the superconducting energy gap.

RBS CHARACTERIZATION

DATA ACQUISITION

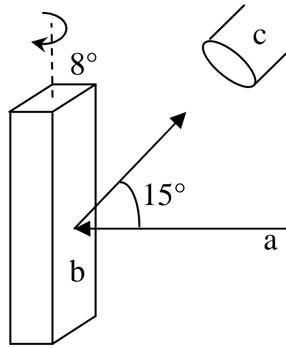

Figure 3: Schematic diagram of the RBS experimental setup inside the chamber. (a) the incoming α–particle beam, (b) the sample to be analyzed, (c) the Silicon surface barrier detector

Rutherford Backscattering Spectroscopy (RBS) is used in this investigation to determine the composition, thickness, and layer structure of the samples. This analysis is performed using the 1.7 MeV Tandetron Accelerator and α -particle beam-line within the LeRoy Eyring Center for Solid State Science at Arizona State

University. This technique uses α -particles accelerated to 3.05MeV (where an α -particle is defined as an He^{2+} ion) impinging at 8° to the normal of the film surface, with 15° between the beam direction and detector position at the sample in a vacuum chamber with pressure of 10^{-7} Torr or better.

The RBS Technique measures the energy and flux of inelastically backscattered atoms using a Silicon Surface Barrier Detector. The particular scattering geometry utilized is Rutherford Backscattering. After the particle-particle interaction, the final energy is governed by the kinematic factor equations: [11]

$$E = k^2 E_0 \tag{7}$$

$$k = \frac{M_i \cos(\theta_1) + \sqrt{M_s^2 + M_i^2 sin^2(\theta)}}{M_i + M_s} \tag{8}$$

Where θ_1 is the scattering angle in the lab frame of reference, M_i is the mass of the incident particle, and M_s is the mass of the sample element. The equation for the probability of a scattering event is given by the differential cross-section:

$$\frac{d\omega}{d\Omega} = \left(\frac{Z_1 Z_2 e^2}{4E_0}\right)^2 \frac{1}{Sin^4\left(\frac{\theta}{2}\right)} \tag{9}$$

Where Z_1 and Z_2 are the atomic numbers of the target and beam elements, and θ is the scattering angle in the mass frame of reference. [12]

This data is recorded by the detector in channels which are translated to energy via E=keV/channel+E_0, where typical settings for this accelerator are 5.45keV/channel and a

channel 0 of E_0=25keV. Data is recorded over a pre-determined number of incident particles (in this case, 2×10^5 counts), where 1 count corresponds to a dose of $\approx2.5\times10^9$ ions/cm^2.

$$Dose\left(\frac{ions}{cm^2}\right) = \frac{counts}{0.1225cm^2 \times 2 \times 1.6 \times 10^{-19}\left(\frac{Coul}{ion}\right) 0.1 \times 10^{11}\left(\frac{counts}{Coul}\right)} \quad (10)$$

or, a total of $\approx3.125\times10^8$ ions for 200000 counts.

RBS DATA ANALYSIS

Results are plotted as yield vs. channel, and then a computer simulation is performed using software packages XRump and Genplot [13] to fit the experimental data. For simple structures, a simulation can be accurate within $\pm5\times10^{15}$ atoms/cm^2 thickness (≈5Å), and ±0.01 at% for composition. Due to the measurement geometry (an aerial atomic count with a finite sized beam), the atoms/cm^2 unit is directly inferred with RBS—this can be converted to a thickness for a film of known density. The front-edge positions of each surface element can be calculated by using the kinematic factor to identify the surface elements. This method has good mass resolution for lighter elements, where we are even able to resolve isotopes of different mass. However, at lower incident beam energies, heavier elements have kinematic factors much closer together since the $\frac{\sqrt{M_s^2+M_i^2 sin^2(\theta)}}{M_i+M_s}$ term of the kinematic factor (Eq. (8)) has smaller differences with larger sample masses, so these can be more difficult to resolve.

Due to electronic interactions with the atoms, the energy of the particles is dissipated as the beam travels through the sample, such that the energy width of each peak corresponds

to the thickness of the layer. This energy loss is from electronic-energy loss; the high-energy charged particle excites electrons and ionizes atoms as it moves through the solid. Macroscopically this is observed as a continuous energy loss through the thickness. Non-surface layers will have their energy shifted down by the same amount as the energy width of the layers closer to the surface. As a result, RBS can simulate multi-layered structures very accurately. Layer thicknesses can be determined to within ±5Å under good conditions, such as smooth, uniform films with known film densities. The number of counts on each channel (yield) corresponds to the atomic concentration of the element, scaled by a correction factor based on the total incident particle dose. From this, atomic concentrations can be inferred to within 0.1 at% if the layer is above a threshold thickness (where the width of the measured peak is large enough for the top to be flat). For thick enough layers and heavy enough elements, the lower detection limit can be as low as 0.05 at%. For light elements (Na and below), the accelerator used is able to reach specific (non-Rutherfordian) Nuclear Resonance Scattering (or NRA–Nuclear Resonance Analysis) energies, where the yield will be very high due to the additional scattering interaction with the nucleus of the target atom. This is simulated within the software only if the incident energy is at or above one of these resonance energies (for example, 3.05MeV for Oxygen), but since measurements for this study were taken at 2.0MeV, NRA is not taken into consideration.

With RBS, the film thicknesses and chemical compositions of the samples were determined.

XRD CHARACTERIZATION

Two X-ray Diffraction (XRD) was performed using of λ =0.154nm Cu-K_α X-rays in the PANAlytical X'Pert MRD diffractometer within the LeRoy Eyring Center for Solid State Science at Arizona State University. This technique is able to determine crystallographic information, lattice spacing, film orientations, texture, stress/strain, able to infer phases present in samples, and determine whether they are single crystal, polycrystalline, or randomly (powder) oriented. X-rays used in these studies have a useful probe depth of ~1μm and beam size of 2mm×10mm.

This investigation used XRD θ-2θ coupled scans to investigate whether any unexpected phases, such as a Mo-Cu phase at the interface, are present, and used XRD rocking curve measurements to determine a relative film crystal quality.

POWDER CONFIGURATION X-RAY DIFFRACTION

The most common geometry for XRD analysis is the "powder diffraction" configuration, which is used for measuring interatomic plane distances (d_{hkl}), where (hkl) is the specific crystallographic index. In this setup, the X-ray beam source and detector move around the sample with angles θ and 2θ relative to the sample surface. As shown in the diagram (Fig. 4), a strong diffraction is only observed at angles where the beam angle corresponds to constructive interference, or when the "Bragg Condition" is met. The Bragg diffraction condition is:

$$n\lambda = 2d_{hkl}\sin(\theta) \tag{11}$$

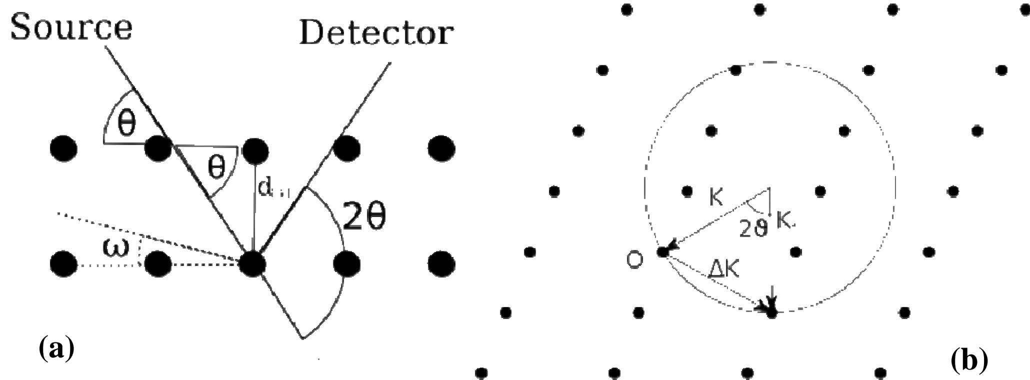

Figure 4: Diagrams of the X-ray Diffraction scan configuration for (a) real-space and (b) K-space. In (a) the black dots represent the atoms of the lattice, and the lines from the source to the detector represent the x-rays. In (b) the black dots represent families of lattice planes, with those along the circle being Bragg reflections.

Where nλ is any multiple of the beam wavelength (in this case 0.154nm), θ is the angle between the beam incident and the sample surface, and d_{hkl} is the lattice spacing for the particular (hkl) index being identified. In K-space, this scan geometry corresponds to rotating the $\overline{K}$ vector around the origin and drawing an Ewald sphere, where each Bragg spot touching the Ewald Sphere is a diffraction where the Bragg condition is met, and corresponds to a peak in the scan. (see Fig. 4b.) Analysis of this scan consists of plotting the detected beam yield against the 2θ angle, and indexing each of the resulting peaks by their respective lattice spacings and corresponding (hkl) value. A cubic structure can be indexed by:

$$d_{hkl} = \frac{a}{\sqrt{h^2 + k^2 + l^2}} \tag{12}$$

Identifying phases is typically performed by comparing the resultant peak to a database of available Powder Diffraction Card Files (PDF cards), listing the possible peaks for each element or compound.

X-RAY ROCKING CURVE

XRD Rocking curve measurements can be used to determine the distribution of planes around a particular 2θ position, and is a relative metric of a film's crystal quality. This measurement is performed in real-space by fixing θ and 2θ around the Bragg condition for the targeted lattice orientation, then rocking the sample by a small angle (ω, as shown in Fig. 4a). In K-Space this corresponds to performing a scan around the selected Bragg Diffraction Spot (along the Ewald circle, Fig. 4b), and measuring the diameter of the Bragg spot.

Both the XRD powder and rocking curve techniques are used in this investigation to determine the crystallographic orientations, identify the phases present, and compare relative crystalline qualities.

ATOMIC FORCE MICROSCOPY

Atomic Force Microscopy (AFM) characterization is useful for obtaining a 3-D topographical map of the sample surface, which will yield information about surface features and roughness. Under optimal conditions, atomic resolution can be achieved all three axes. The technique works by bringing a sharp probe tip near enough to the surface to experience the van der Waals forces. The probe is held by a cantilever connected to a piezoelectric positioning device with a force-feedback circuit to measure the height of the sample surface, and adjust the lever height without crashing the tip into the sample surface. The probe tip is rastered across the surface, a data point (in z -height, in Å) is recorded for each (x,y) position, and then the data are stitched together into an image by the computer.

There are different available modes of operation, where the surface tip is kept outside of the repulsive force region (non-contact mode), within the repulsive force region (contact-mode), or oscillating just above the repulsive force region (tapping mode). Tapping mode is used in this study to get the highest resolution image without damaging the probe tip or the sample surface.

The AFM technique was used to analyze the surface roughness of the film bilayers.

THEORETICAL T_C MODELING

A theoretical simulation of the bilayer T_C and the proximity effect is performed using the Usadel model, based on BCS Theory. BCS Theory is the Nobel-Prize winning theory used to model the superconducting properties of superconductors, developed by John Bardeen, Leon Cooper, and Robert Schrieffer [14]. The Usadel [4] equations are a simple generalization of BCS Theory for metallic bilayers, and of the equations described by Werthamer [3] regarding the proximity effect. The equations used for this simulation are:

$$T_C = T_C(Mo)[\frac{d_{Mo}}{d_\circ} \times \frac{1}{1.13\left(1+\frac{1}{v}\right) \times t}] \tag{13}$$

$$\frac{1}{d_\circ} = \frac{\pi}{2} k_B T_C(Mo) \times \lambda_F^2 n_{Mo} \tag{14}$$

$$v = \frac{d_{Cu} n_{Cu}}{d_{Mo} n_{Mo}} \tag{15}$$

Where T_C is the resulting bilayer superconducting transition temperature, $T_C(Mo)$ =0.9K [7]is the T_C of Mo, d_{Mo} and d_{Cu} are the thicknesses of Mo and Cu respectively in Å . k_B is the Boltzmann constant in eV/K , λ_F is the Fermi wavelength. In this case the λ_F value

for Copper is used-- and is λ_F=0.462nm. $n_{Mo}=0.29\times10^{23}$ states/eVcm^3 and $n_{Cu}=0.125\times10^{23}$ states/eVcm^3 are the density of electronic states for Mo and Cu, respectively, and finally, t is the interface transmission coefficient, which is a relative "quality" of the interface, where a better interface has a higher t -value.

These equations are plotted along with the thickness and T_C data points, and the interface transmission coefficient is compared to points on the graph in order to fit an interface transmission coefficient (t) curve with each data point.

In summary, the Usadel equations were used to model the expected T_C vs. thickness curves, and to determine the different interface transmission coefficients, t, for each film that did not fit along the theoretical line.

CHAPTER 3

RESULTS & DISCUSSION

For this section of the document, results from each characterization technique are presented in order of being performed. This allows for a chronological discussion of conclusions that were drawn over the course of research, and helps give insight as to why the particular techniques were chosen. For the readers' convenience, samples will be referred to by their approximate Mo thickness, as measured by RBS, instead of by long and potentially cryptic internal sample numbers.

ELECTRICAL CHARACTERIZATION

The Residual Resistivity Ratio (RRR) allows for a qualitative comparison of electronic properties. Resistivity and RRR properties are important for device thermalization time and our targeted coherence length of ξ_{Cu}=1000Å for the predicted proximity effect behavior. These restrictions impose a targeted RRR≈10. This test can be performed quickly and easily when compared to the expensive and time-consuming T_C measurement that need to be cooled down to 50mK with a dilution refrigerator. Low values of RRR help diagnose problems with the growth process by pointing out samples that have unexpected scattering.

Mo Thickness (Å)	**RRR (±0.1)**
950	12.3
900	12.7
860	11.9
800	12.1
780	11.3
680	13.7

Table 1: Mo thickness and resistivity ratio (RRR 300/4.2K) for Unifilm bilayers with d_{Cu}≈2100±60Å

Measured Mo Thickness (Å)	Transition Temperature T_c (mK)
950	177
900	208
860	120
800	70
780	61
680	<50*

Table 2: Superconducting transition temperatures for Unifilm bilayers *Sample did not exhibit superconductivity above the 50mK measurement minimum

The results show that each of the RRR values is above the value of 10 necessary to achieve a long coherence length of $\xi \geq 1000$Å. Since the Cu layer thickness is ≈2150Å, we can know that the film is electrically thick enough, thickness>2ξ, it is above the limit for the proximity effect, and small variations will not affect the bilayer T_C. After RRR measurements, portions of each bilayer wafer were sent to NIST for T_C measurement, and portions to ASU for further characterization.

The T_C measurement shows a general trend in which T_C increases as the thickness of the superconducting Mo layer is increased, as is expected. Since the Cu layer thickness is kept constant, there will be higher density of cooper pairs (and as such, higher T_C) as we approach a layer thickness on the order of ξ_{Mo}, after which the T_C will stop increasing with thicker Mo layers.

RUTHERFORD BACKSCATTERING SPECTROSCOPY (RBS)

Rutherford Backscattering Spectroscopy (RBS) is used to characterize the layer thicknesses, look for any large-scale intermixing, and identify any contaminants. Some

Target Mo Thickness (Å)	Actual Mo Thickness (±5Å)	Measured Cu Thickness (±5Å)	Ar Content (atoms$\times10^{15}$/cm^2)
1000	950	2100	46.2
950	900	2130	86.5
850	860	2070	14.7
800	800	2110	10
750	780	2100	4.71*
650	680	2160	0.37*

Table 3: Approximate thickness and Ar content for each film bilayer. The target thickness for all Cu layers was d_{Cu}=2150Å. A 0* indicates no signal above background noise suitable for peak integration (below detection limit) so the integration above computer-calculated background was used. Ar content is simulated to be near the bottom ≈30Å of Mo.

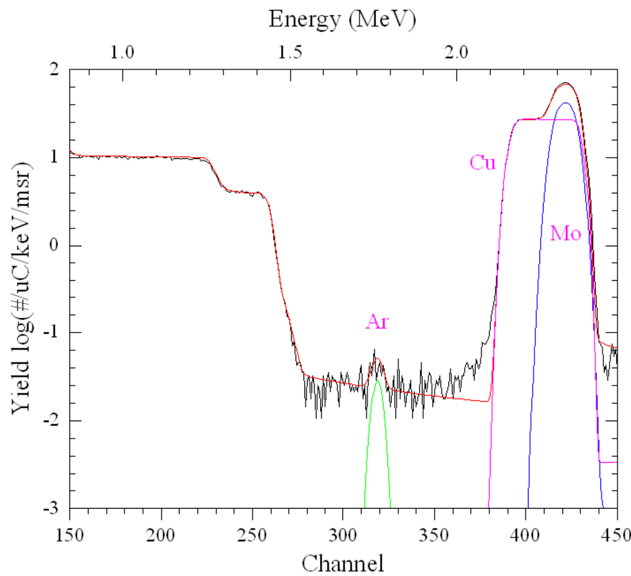

Figure 5: Simulated RBS data for Mo 900 shown in the log scale. The argon peak is visible above the baseline

bilayers are found to contain Argon contamination, but no other contaminants were observed.

RBS results were obtained using a Tandetron accelerator with 3.05MeV α-particles incident at 8° normal to the sample surface. Data were collected for 2×10^5 counts, and simulated using Rump [13]. A

typical simulated data plot (for a sample containing argon) is shown in Figure 5.

The thickness of each elemental layer is determined as the full-width-half-maximum (FWHM) of the peak, and the depth at which the element occurs from the surface is identified by how far below the theoretical front-edge energy the onset of the peak appears. In the example plot above, the Cu and Mo peaks add to each other to form the resultant peak visible. The Mo peak is pushed back from its typical front edge, and the Cu peak begins at its theoretical front edge. Therefore, even without any prior knowledge of the sample, we can determine that the Cu resides at the sample surface, and the Mo begins at a depth of ≈2150Å (corresponding to the FWHM of the Cu peak). We can then see that the Si in the SiO_2 substrate is shifted from its typical front edge by the sum of the widths of the Cu and Mo peaks. This indicates that there are three distinct layers, Mo, Cu, and SiO_2, and the simulations do not suggest any intermixing between the layers.

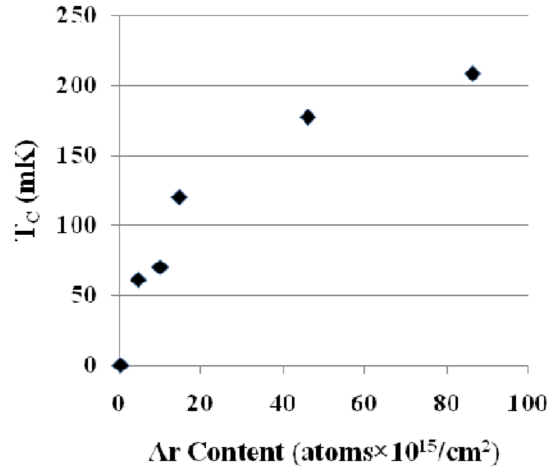

Figure 6: Bilayer T_C and argon content from RBS shows a positive trend. This does not consider thickness

While typically, data analysis for RBS is plotted with linear yield, it is useful to refine simulations in the logarithmic scale when searching for low-concentration contaminants. This allows for observation of peaks which may be much smaller than the main element peaks, and in this case detect argon.

It is evident from the position of the Ar peak, that there is Ar present in some of the Mo layers, but not in the Copper top layer. The shift from its typical front edge indicates that when Ar is present, it does not appear until very near the Mo-substrate interface. Since the Ar is not present through the entire thickness of the Mo layer, the Ar peak FWHM is very small. Since the atomic percentage is also small, the intensity is low. This makes quantifying the Ar content more difficult. The best way to get the total Ar content was to integrate the total Ar peak area, giving units of atoms$\times 10^{15}$/cm^2, as shown in Table 3. Bilayer argon content correlates with the measured T_C of the samples, as shown in Figure 6. This suggests that argon content may play a role in the final T_C of the bilayers.

The RBS measurement probes a sample area approximately 3mm$\times$3mm. Because RBS peak shapes at the back-edge are Lorentzian, it can be difficult in thin layers to distinguish whether tails are from layer intermixing, surface roughness, or typical energy straggle.

RBS was used to determine the layer thickness, screen for large-scale layer intermixing, and identify contaminants. Argon contamination was discovered in a number of samples.

X-Ray Diffraction (XRD) can be used to determine lattice spacings, crystal orientation, crystal structures, and strain present in the sample. While the Mo has a predominantly polycrystalline (110) orientation normal to the surface, the Cu layer exhibits both Cu (111) and (110) orientations normal to the

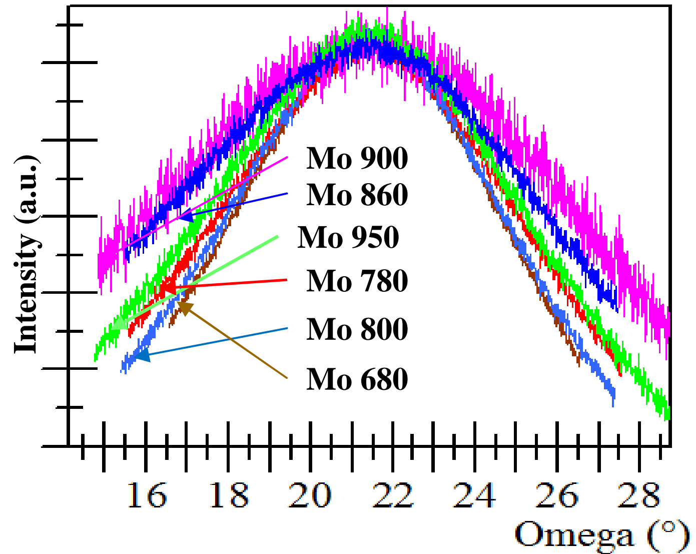

Figure 8: XRD Rocking Curve data for the Cu (111) peak of each sample, normalized to the maximum peak height. Difference in FWHM between samples is easily seen. Sample labels ordered from largest to smallest FWHM.

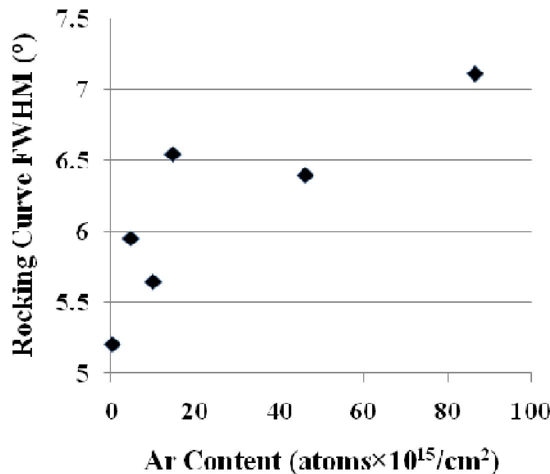

Figure 7: Rocking Curve FWHM for Cu (111) and argon content from RBS shows a small, but positive trend. Please note the y-axis origin is not at zero.

surface. XRD rocking curve measurements were performed on the Cu (111) peak, and these data show that a lower crystal quality (larger peak FWHM) correspond with higher Argon contamination (as determined by RBS), visible in Figure 7.

Due to the x-ray penetration depth being much longer than the thickness of the sample, and the strong scattering ability of the single crystal Si (100) substrate, the θ-2θ

scans were performed with a small ω-offset from the sample normal to avoid the data being washed-out by the large Si substrate (400) peak. The primary Si (400) peak position is at 69.5° (in 2θ), which is outside the chosen scan range for these Mo/Cu bilayers. The peaks observed were at 40.5°, 41.5°, 43.3°, and 50.4°. To identify these peaks, the International Centre for Diffraction Data (ICDD) database was searched for all likely materials and compounds. By comparing peak position with those in the database, the Mo (110) at 40.51°, Cu (111) at 43.29°, and Cu (200) at 50.43° orientations were identified in the samples, with an additional cluster of CuO_x peaks near 41.5°.

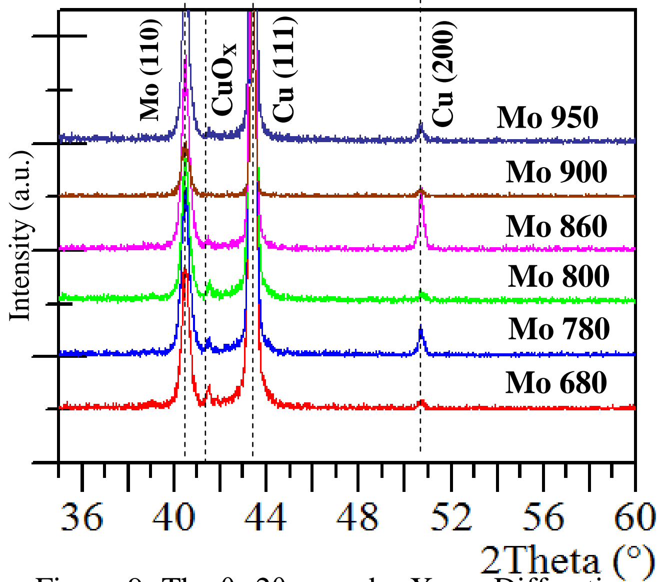

Figure 9: The θ -2θ powder X-ray Diffraction plots for each of the film bilayers. The observed peaks are Mo (110) at 40.51°, Cu (111) at 43.29°, Cu (200) at 50.43°, and a cluster of CuO_x peaks near 41.5°.

Strain has been shown to enhance T_C of superconducting materials, specifically, thin films of Mo have been measured with T_C as high as 3.3K [15] (compared to the bulk T_C value for Mo of 0.9K. This is significant because it could lead to very different original T_C values for our Mo films, affecting the final bilayer T_C. The XRD θ-2θ measurement was used to approximate differences in strain between bilayers. In order to approximate strain in the Mo, deviation in d-spacing (based on the Mo (110) peak) was used to estimate relative strain. The highest relative strain measured was 0.03% , and the lowest 0.01%. These values are likely too small to affect the T_C of Mo films significantly [16]. This type of

analysis does not reflect the true strain in the films, but is an approximation adequate for this study. Due to the measurement geometry, it considers only the change in d-spacing perpendicular to the surface. A more accurate strain measurement can be done by strain-m aping an in-plane peak (requires reciprocal space mapping), or by performing a $\sin^2\Psi$ analysis on the Mo(110) peak, but both techniques require significant additional work that was not performed as part of this study.

These results indicate that the Mo sputter growth yields a well-oriented film, with only one crystallographic orientation, and no significant strain present. The Cu film has a primary (111) orientation, with some (200) oriented grains, and some additional CuO_x peaks, likely from surface oxidation. No additional peaks were observed, and no phases indicative of intermixing or chemical reaction between the film layers were identified. A Mo-Ar phase was searched for, but not detected.

ATOMIC FORCE MICROSCOPY (AFM)

Atomic Force Microscopy (AFM) was used to measure surface roughness of each sample. A sample without any detected Ar (Mo 680) shows RMS Roughness of 1.66nm, while the sample with highest detected Ar content has a surface roughness of 7.08nm. This roughness also correlates with the XRD rocking curve result for relative film quality The low roughness film corresponds to the smallest rocking curve

Mo Thickness (Å)	**RMS Roughness (±0.01 nm)**
680	1.66
780	2.85
800	3.65
860	3.105
900	7.08
950	3.71

Table 4: The RMS surface roughness for each film bilayer, measured by AFM.

FWHM (highest "quality") and the high roughness sample is the largest FWHM (lowest "quality"). The AFM surface roughness results also correlate with the argon content, as measured by RBS, and shown in Figure 11.

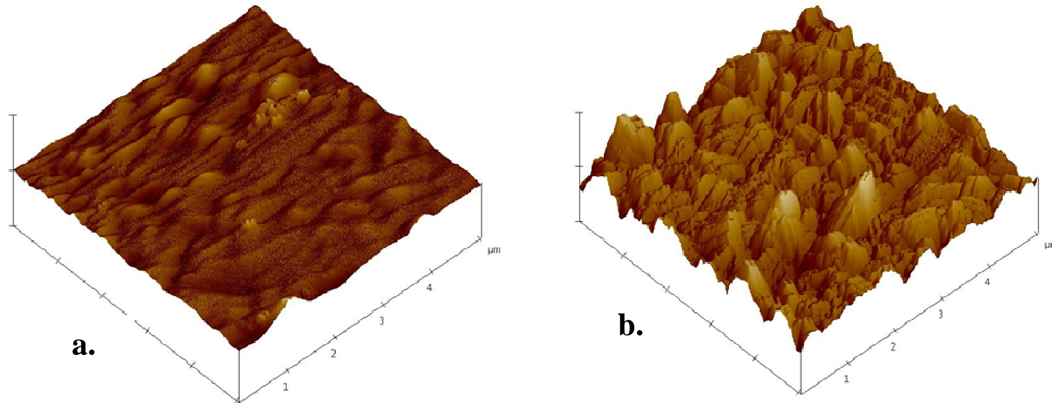

Figure 10: Shows the difference in roughness and surface features for a sample with no Argon contamination, and the sample with the highest argon contamination. (a) 3-D AFM Image for Unifilm Mo 680 showing RMS roughness 1.66nm. (b) 3-D AFM Image for Unifilm Mo 900 showing RMS Roughness 7.08nm.

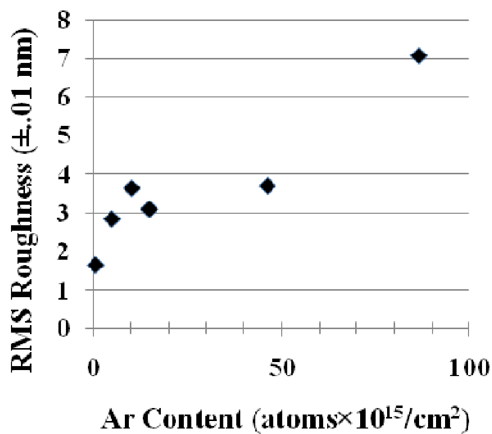

Figure 11: RMS surface roughness and measured argon content exhibit a positive correlation.

The roughness of the sample generally correlates to the relative quality of the film, and these results match the relative qualities determined by X-ray Rocking Curve. Since the Cu top layers are free of contaminants, and the same process is used for each Cu deposition, the roughness is likely transferred from the Mo/Cu interface, and could be representative of Mo roughness. Work by Ali, et al. [6] shows that higher Argon pressure during sputtering increases the incorporation of Ar into the growing film, and causes a lower RRR_{Mo}. In

the future, it would be interesting to investigate the relationship between incorporated Argon content and surface roughness of single-layer Mo films.

AFM was used to determine the surface roughness of Mo/Cu film bilayers. It was discovered that the thinnest bilayer, containing no Ar, has lower roughness than the bilayer with highest detected Ar content.

T_C SIMULATION

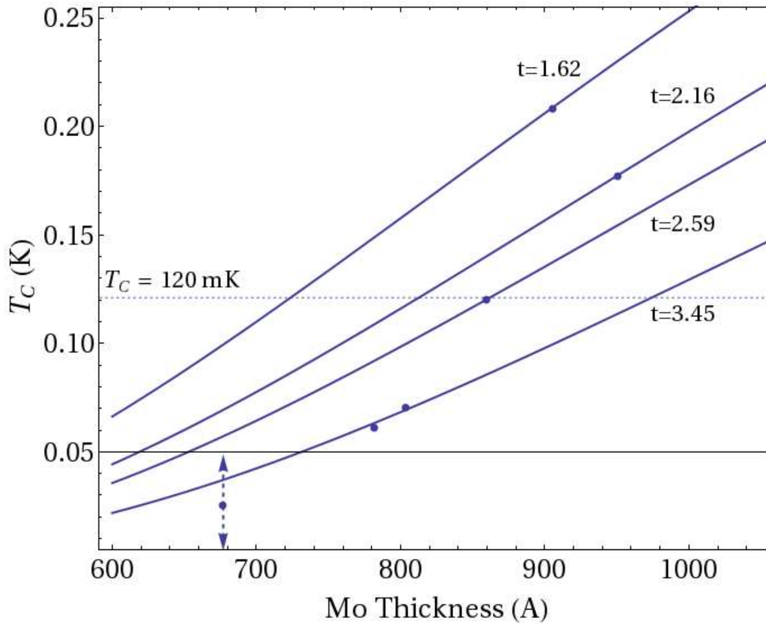

Figure 12:Usadel simulations for each bilayer. A dashed line at 120mK shows the targeted T_C for the device, and the vertical dashed line at d_{Mo}=680Å represents the sample which did not superconduct above the 50mK minimum temperature for the equipment. It is assumed that it will superconduct at some temperature below the measurement limit.

The Usadel equations were used to simulate the structures used in this study. The simulation used values for layer thickness determined by RBS, and the interface transmission coefficient, t, was varied to find values that fit with experimental T_C data. For these simulations, a T_C(Mo)=900mK was assumed, based on literature results for Mo of similar thickness [16]. This does not take into account the effect that differences in strain would have on the single film T_C, but was necessary to make since measuring the T_C of these Mo films without the influence of the

Cu was not possible. It is shown in Figure 8 that the samples do not all fit along the same curve. This suggests that the interface transmission coefficient (sometimes called interface transparency), is different for these samples. This difference appears to be correlated with the measured argon content, different surface roughness, and the Cu rocking curve FWHM, as shown in Figure 13.

In Figure 12, the interface transmission coefficient has been chosen to cause the simulation to fall along the T_C data for each sample. Because T_C measurements at NIST could not be performed below 50mK, and one sample is at or below that limit, it was plotted on the limiting line. The lines of different interface transmission coefficients correlate with a lower t for lower relative quality, which matches the correlations made with Ar content, XRD Rocking Curve, and AFM.

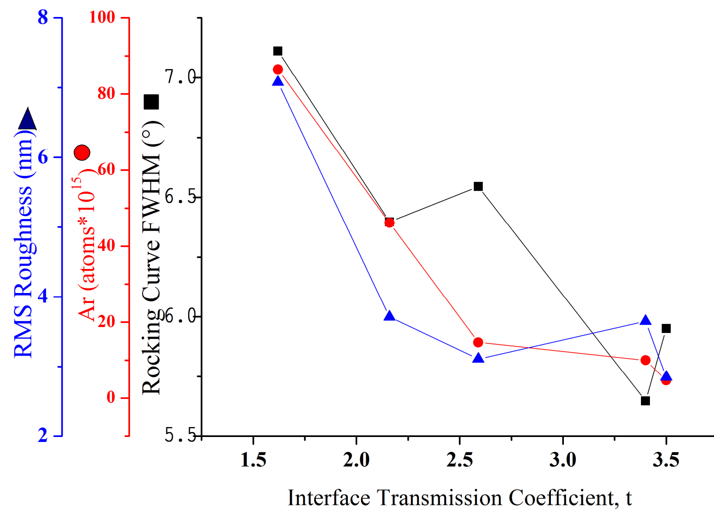

Figure 13: Shows negative correlation between t and; Ar content, RMS roughness, and rocking curve FWHM.

CONCLUSIONS

A number of Mo/Cu film bilayers are fabricated using sputtering, and characterized for their superconducting T_C, resistivity ratio, thickness and argon content, crystal structure properties, and surface roughness. To compare with theory, the Usadel model was used to infer different interface transmission coefficients (t) for each sample. Argon was detected by RBS at the Mo-substrate interface. Correlation between the argon content in the Mo-substrate interface and the value for t suggests that argon is a factor in the deviations from expected T_C. This is best exhibited in Figure 13 where the correlation between t and the Ar content (as determined by RBS), Cu (111) rocking curve FWHM, and the bilayer surface roughness (determined by AFM). Bilayers were determined to be clean and free of other contaminants, and do not exhibit any indication of intermixing or reacting at the Mo-Cu interface by either RBS or XRD θ-2θ techniques. XRD Rocking curve measurements indicate that the crystalline quality of the copper layer trend with the t-value, similarly to the AFM bilayer surface roughness. It is inferred by the d-spacing perpendicular to the surface, that strain does not play a large part in modifying the T_C. By inferring that the film bilayer surface roughness is a feature caused by roughness at the Mo-Cu interface, it can be assumed that interface roughness affects the crystalline quality of top Cu layers, and these contribute to the change in t value. The plasma pre-sputter that is used to clean the substrates before deposition likely causes this argon at the substrate-Mo interface. Preventing that initial high concentration of argon by using a different ion for sputter cleaning, or using a different substrate cleaning technique, could solve the T_C deviation problems. Furthermore, during the course of this study, a bilayer of the desired T_C (120mK) was produced, so the study is considered a success.

Further interesting work should include a systematic study of single-layer Mo-films to investigate the role Ar-incorporation plays in Mo-surface roughness, strain, and the electrical properties of the Mo-layer. Discovering the cause of the difference in argon content, or a method to prevent its incorporation in films, would be of practical use to the commercial manufacture of these devices. It may be useful to attempt sputtering with a heavier ion, such as krypton or xenon, to avoid ion incorporation in the films.

REFERENCES

1. **Irwin, K.D, Hilton, G.C.** Transition Edge Sensors. [book auth.] Christian Enss. *Cryogenic Particle Detection.* s.l. : Springer Berlin Heidelberg, 2005, pp. 63-150.

2. *Proximity effect in iridium-gold bilayers.* **Nagel, U. and al, et.** 7, s.l. : Journal of Applied Physics, 1994, Vol. 76, pp. 4262-4266. doi:10.1063/1.357310.

3. *Theory of the superconducting transition temperature and energy gap function of superposed metal films.* **Werthamer, N. R.** 6, 1963, Physical Review, Vol. 132. doi:10.1103/PhysRev.132.2440 .

4. *Generalized Diffusion Equation for Superconducting Alloys.* **Usadel, K.D.** 8, s.l. : Physical review letters, 1970, Vol. 25. doi:10.1103/PhysRevLett.25.507.

5. *A Mo–Cu superconducting transition-edge microcalorimeter with 4.5 eV energy resolution at 6 keV.* **Irwin, K.D.** 1-2, 2000, Nuclear Instruments and Methods in Physics Research Section A, Vol. 444. doi:10.1016/S0168-9002(99)01354-6.

6. *Fabrication of Mo/Cu Multilayer and Bilayer.* **Ali, Z. A.** 2, 2005, IEEE TRANSACTIONS ON APPLIED SUPERCONDUCTIVITY, Vol. 15. doi:10.1109/TASC.2005.849897.

7. **Lide, D.R., [ed.].** *CRC Handbook.* 87. s.l. : CRC Press, 2006.

8. **Subramanian, P. R. and Laughlin, D. E.** Cu-Mo. [book auth.] T. B. Massalski. *Binary Alloy Phase Diagrams.* s.l. : ASM International, 1990, pp. 1435-1438.

9. *Modelling the energy gap in transition metal/aluminium bilayers.* **Brammertz, G.** 3-4, 2001, Physica C: Superconductivity, Vol. 350. doi:10.1016/S0921-4534(00)01607-5.

10. *Normal electron-electron scattering in thin films at low temperatures: Anomalous surface impedance.* **Movshovitz, D., Wiser, N.** 10503, 1990, Phys. Rev. B, Vol. 41. doi:10.1103/PhysRevB.41.10503 .

11. **Alford, T.** *Fundamentals of Nanoscale Film Analysis.* s.l. : Springer, 2007. p. 14. ISBN: 978-0-387-29260-1.

12. **Oura, K. et al.** Surface Science: An Introduction. s.l. : Springer, 2010, p. 110.

13. **Thompson, M.** RUMP and Genplot. [software]. s.l. : GENPLOT. http://genplot.com.

14. *Theory of Superconductivity.* **J. Bardeen, L. N. Cooper, and J. R. Schrieffer.** 1175, s.l. : Phys. Rev, 1957, Vol. 108. doi:10.1103/PhysRev.108.1175.

15. *Electrical Properties and Superconductivity of Rhenium and Molybdenum Films.* **Frieberthauser, P.E. and Notarys, H.A.** 4, s.l. : Journal of Vacuum Science and Technology, 1970, Vol. 7, pp. 485 - 488 . doi:10.1116/1.1315371.

16. *Mo-Based Proximity Bilayers for TES: Microstructure and Properties.* **Fàbrega, Lourdes and et.al.** 3, s.l. : Applied Superconductivity, IEEE Transactions on, 2009, Vol. 19, pp. 460 - 464. doi:10.1109/TASC.2009.2019052.